Available online at www.sciencedirect.com
SCIENCE DIRECT®
Journal of Computational Physics 195 (2004) 695–717
JOURNAL OF COMPUTATIONAL PHYSICS
www.elsevier.com/locate/jcp

Spectral distributed Lagrange multiplier method: algorithm and benchmark tests

Suchuan Dong, Dong Liu, Martin R. Maxey, George Em Karniadakis *

Division of Applied Mathematics, Center for Fluid Dynamics, Brown University, Providence, RI 02912, USA

Received 6 May 2003; received in revised form 23 September 2003; accepted 10 October 2003

Abstract

We extend the formulation of the distributed Lagrange multiplier (DLM) approach for particulate flows to high-order methods within the spectral/*hp* element framework. We implement the rigid-body motion constraint inside the particle via a penalty method. The high-order DLM method demonstrates spectral convergence rate, i.e. discretization errors decrease exponentially as the order of spectral polynomials increases. We provide detailed comparisons between the spectral DLM method, direct numerical simulations, and the force coupling method for a number of 2D and 3D benchmark flow problems. We also validate the spectral DLM method with available experimental data for a transient problem. The new DLM method can potentially be very effective in many-moving body problems, where a smaller number of grid points is required in comparison with low-order methods.

1. Introduction

Existing numerical methods for simulating particle-flow interactions can be broadly classified into two categories. The first category is Lagrangian methods, in which the grid follows the fluid. The arbitrary Lagrangian–Eulerian (ALE) [12,13] technique and the space–time finite element methods [16,17] belong to this category. The ALE particle mover uses a technique based on a combined fluid particle momentum equations, together with an ALE moving unstructured finite element mesh to deal with particle movement. In the space–time approach, the temporal coordinate is discretized with finite element methods along with the spatial coordinates, and the deformation of the spatial domain with time is reflected simply in the deformation of the mesh in the temporal coordinate. The ALE finite element scheme can be framed as a

* Corresponding author. Fax: +1-401-863-3369.
E-mail address: gk@dam.brown.edu (G.E. Karniadakis).

0021-9991/$ - see front matter
doi:10.1016/j.jcp.2003.10.016

special case of the space–time method [1,10]. While these methods are capable of handling particles of different shapes, sizes and materials, the overhead of constant re-meshing the flow domain can be significant. Typically, several hundred particles (up to 1000 in [17]) can be simulated with this approach, but scaling the problem higher is computationally expensive.

In the second category of methods, flow computations are conducted on a fixed grid while the particle movement or deformation is accounted for by certain constraints [2,8,26,27,32], interaction equations [4,22,37] or front tracking/capturing technique [42]. The force coupling method (FCM) [26,27] represents the particles by low-order force multipoles distributed over a finite volume; such force multipoles are included as body force terms in the Navier–Stokes equations. The immersed boundary method was initially introduced to study flow patterns around heart valves [35,36] and has evolved into a generally useful method for problems of fluid–structure interactions [3,4]. In this method, the flow equations are discretized on a fixed Cartesian mesh while the immersed boundary is represented by Lagrangian variables defined on a curvilinear mesh that move freely through the fixed Cartesian mesh. The two sets of representations are linked through the interaction equations with a discrete delta function [37]. Another method is implemented in *Physalis* proposed by Prosperetti and Oguz [38]; it uses an analytical solution in the neighborhood of each particle and matches this solution to the external flow field calculated numerically. On the other hand, for the liquid–liquid or gas–liquid two-phase flows, a large number of front-capturing and front-tracking methods exist that fall into this category, e.g. the marker-and-cell (MAC) method, the volume-of-fluid (VOF) method [39], level set method [28,41], constrained interpolation profile method [43], the phase field method [14,15] and the front tracking method [5,42]. The methods in the second category are generally more efficient because the computations are carried out on a fixed grid.

The distributed Lagrange multiplier (DLM) method [2,6–8,29,32–34] (in [2] it is called virtual finite element method), which this paper focuses on, falls into the second category. With the DLM method, the problem on a time-dependent geometrically complex domain is extended to a stationary, larger, but simpler domain so that a fixed mesh can be used. The no-slip boundary conditions between the particles and the fluid are satisfied through the constraints of rigid-body motion of the fluid in the volume of particles. These constraints are enforced through DLMs, which represent the additional body force required to maintain the rigid-body motion inside the particle. The original DLM algorithm [6–8] with the velocity-based rigid-body motion constraint is not readily applicable to neutrally buoyant particles. To overcome this, a strain-rate based constraint was proposed in [32], which was suitable for both non-neutrally buoyant and neutrally buoyant particles. Recently, Pan and Glowinski [29] have generalized the formulation of velocity-based constraints in [8] to cases involving neutrally buoyant particles by adding extra conditions to the space of Lagrange multipliers. The DLM method has been applied to study sedimentation [30], fluidization [31], and viscoelastic particulate flows [40] with the number of particles reaching the order of 1000–10,000 in 2D and 100–1000 in 3D.

All the above DLM approaches are formulated based on the finite element method with linear elements, except in [18] where Taylor–Hood finite elements are used. In the current paper we extend the formulation of DLMs to the spectral and spectral/*hp* element methods, and enforce the rigid-body motion constraint with a penalty approach [11]. A stiffly-stable high-order scheme is employed for the integration in time [19]. We demonstrate that the resulting spectral DLM method achieves exponential convergence. The objectives of this paper are to present the spectral DLM formulation and evaluate its performance and accuracy by systematic comparisons with direct numerical simulations and with the FCM for a number of 2D and 3D benchmark flow problems.

This paper is organized as follows. In Section 2 we present the spectral DLM approach. In Section 3 a brief summary of the FCM is provided. In Section 4 we quantify the accuracy and convergence behavior of the spectral DLM method and present comparisons with other methods using similar discretizations. We conclude in Section 5 with a summary and some remarks.

2. Spectral DLM method

Consider a 3D flow region Ω containing N_p particles $P_1, P_2, \ldots, P_{N_p}$. The combined particle–fluid system is described by a system of differential-algebraic equations [8] as follows:

$$\begin{aligned}
&\rho_{\mathrm{f}} \int_{\Omega} \left[\frac{\partial \vec{u}}{\partial t} + (\vec{u} \cdot \nabla)\vec{u} - \vec{g} \right] \cdot \vec{v} \, \mathrm{d}\vec{x} - \int_{\Omega} p \nabla \cdot \vec{v} \, \mathrm{d}\vec{x} + 2\mu \int_{\Omega} \vec{\vec{S}}(\vec{u}) : \vec{\vec{S}}(\vec{v}) \mathrm{d}\vec{x} \\
&\quad + \sum_{j=1}^{N_p} \left(1 - \frac{\rho_{\mathrm{f}}}{\rho_j} \right) \left[M_j \left(\frac{\mathrm{d}\vec{V}_j}{\mathrm{d}t} - \vec{g} \right) \cdot \vec{Y}_j + \left(\vec{\vec{I}}_j \cdot \frac{\mathrm{d}\vec{\omega}_j}{\mathrm{d}t} + \vec{\omega}_j \times \vec{\vec{I}}_j \cdot \vec{\omega}_j \right) \cdot \vec{\Theta}_j \right] \\
&\quad = \sum_{j=1}^{N_p} \langle \vec{\lambda}_j, \vec{v} - \vec{Y}_j - \vec{\Theta}_j \times (\vec{x} - \vec{G}_j) \rangle_j + \int_{\partial \Omega_{\mathrm{N}}} \vec{n} \cdot \vec{\vec{\sigma}} \cdot \vec{v} \, \mathrm{d}s, \quad \forall \vec{v} \in (H_0^1(\Omega))^3, \ \forall \vec{Y}_j \in \mathbb{R}^3, \ \forall \vec{\Theta}_j \in \mathbb{R}^3,
\end{aligned} \tag{1}$$

$$\int_{\Omega} q \nabla \cdot \vec{u} \, \mathrm{d}\vec{x} = 0, \quad \forall q \in L^2(\Omega), \tag{2}$$

$$\langle \vec{\mu}_j, \vec{u}(t) - \vec{V}_j(t) - \vec{\omega}_j(t) \times (\vec{x} - \vec{G}_j) \rangle_j = 0, \quad \forall \vec{\mu}_j \in \Lambda_j(t), \ \forall j = 1, \ldots, N_p, \tag{3}$$

$$\frac{\mathrm{d}\vec{G}_j}{\mathrm{d}t} = \vec{V}_j, \quad \forall j = 1, \ldots, N_p. \tag{4}$$

In the above equations, $H_0^1(\Omega) = \{ w \in H^1(\Omega) | w = 0 \text{ on } \partial\Omega_{\mathrm{D}} \}$, and $\vec{x}$ and t are spatial and temporal coordinates, respectively. $\partial\Omega_{\mathrm{D}}$ and $\partial\Omega_{\mathrm{N}}$ represent Dirichlet and Neumann boundaries of the domain, respectively. $\vec{u}(\vec{x}, t)$ and $p(\vec{x}, t)$ are flow velocity and pressure, respectively. $\vec{\vec{\sigma}}$ is the stress tensor, $\vec{\vec{\sigma}} = -p\vec{\vec{\delta}} + 2\mu\vec{\vec{S}}(\vec{u})$, where $\vec{\vec{\delta}}$ is the unit tensor. $\vec{V}_j(t), \vec{G}_j(t), \vec{\omega}_j(t), \vec{\lambda}_j(\vec{x}, t)$, $(j = 1, \ldots, N_p)$ are the particle velocity, position, angular velocity and the Lagrange multiplier, $\vec{\lambda}_j \in \Lambda_j(t)$. $\Lambda_j(t)$ is the space of Lagrange multipliers, $\Lambda_j(t) = (H^1(P_j(t)))^3$, $j = 1, \ldots, N_p$. Here, $\langle \cdot, \cdot \rangle_j$ denotes the inner product in the region occupied by particle $P_j(t)$. Also, ρ_{f} and μ are fluid density and viscosity, respectively, which are assumed to be constant; $M_j, \rho_j, \vec{\vec{I}}_j$ are particle mass, density, and the mass moment of inertia, respectively. Finally, $\vec{g}$ represents a body force such as the gravity, $\vec{\vec{S}}(\vec{u})$ is the strain rate tensor, and $\vec{\vec{S}}(\vec{u}) = (\nabla\vec{u} + (\nabla\vec{u})^{\mathrm{t}})/2$. Eq. (1) represents the combined fluid–particle momentum balance. Eq. (2) is the continuity equation. Eq. (3) represents the constraint of rigid-body motion in the region occupied by particles. Eq. (4) is the particle kinematic relation.

The large number of constraints imposed, especially in the presence of many particles, may make the above differential-algebraic system quite stiff. To reduce its computational complexity we enforce the rigid-body motion constraint through a penalty method [11] as follows:

$$\frac{\partial \vec{\lambda}_j}{\partial t^*} + \tau(\vec{u} - \vec{V}_j - \vec{\omega}_j \times (\vec{x} - \vec{G}_j)) = 0, \quad j = 1, \ldots, N_p, \tag{5}$$

where τ is the penalty parameter, t^* is a pseudo time, and $\vec{\lambda}_j$ is the Lagrange multiplier.

We discretize the above system with the hybrid spectral/*hp* element method [20], using a finite-dimensional functional space V^δ for the flow variables. In the spectral/*hp* element method we have two discretization approaches as denoted by h (element size) and the N_{order} (polynomial order on the element). We therefore interpret the use of δ in V^δ to refer to these discretization parameters, and so δ may be thought of

as being a function of h (or similarly the number of spectral elements, N_{el}) as well as N_{order}, that is, $\delta = \delta(N_{\mathrm{el}}, N_{\mathrm{order}})$. Therefore, V^δ is the set of globally continuous functions that are polynomials of order N_{order} on each element. In solving the Navier–Stokes equations we split the pressure and velocity fields in the Stokes problem, which, along with the rotational pressure boundary conditions given in [19,20], leads to unique solutions of the pressure [20]. This approach does not require the use of staggered grids for high-order elements or the use of polynomials with orders lower than those for the velocity to approximate the pressure. Theoretical justification for this is provided in Minev [24] and Guermond and Shen [9]. Similar to [8], we enforce the rigid-body motion of the particle on a set of "collocation points", $\{\vec{x}_i\}_{i=1}^{N_j}$, within the region occupied by each particle $P_j(t)$, $j = 1, \ldots, N_p$, that is,

$$\Lambda_j^\delta(t) = \left\{ \mu^\delta | \mu^\delta = \sum_{i=1}^{N_j} \vec{\mu}_i \delta(\vec{x} - \vec{x}_i), \vec{\mu}_i \in \mathbb{R}^3, \forall i = 1, \ldots, N_j \right\}, \quad \forall j = 1, \ldots, N_p, \tag{6}$$

where $\delta(\vec{x})$ is the Dirac function. The following form of $\langle \cdot, \cdot \rangle_j^\delta$ will be used

$$\langle \vec{\mu}^\delta, \vec{v}^\delta \rangle_j^\delta = \sum_{i=1}^{N_j} \vec{\mu}_i \cdot \vec{v}^\delta(\vec{x}_i), \quad \forall \vec{\mu}^\delta \in \Lambda_j^\delta(t), \ \ \vec{v}^\delta \in V^\delta,$$

$$\langle \vec{\mu}^\delta, \vec{\lambda}^\delta \rangle_j^\delta = \sum_{i=1}^{N_j} \vec{\mu}_i \cdot \vec{\lambda}_i, \quad \forall \vec{\mu}^\delta \in \Lambda_j^\delta(t), \ \ \vec{\lambda}^\delta \in \Lambda_j^\delta(t).$$

Therefore, we express the spectral/*hp* element discretization of the system described by Eqs. (1)–(4) as follows:

Find $\vec{u}^\delta$, p^δ, $\vec{V}_j$, $\vec{G}_j$, $\vec{\omega}_j$, $\vec{\lambda}^\delta$, $\forall j = 1, \ldots, N_p$ such that

$$\begin{aligned} &\int_\Omega \left[\rho_{\mathrm{f}} \left(\frac{\partial \vec{u}^\delta}{\partial t} + \vec{u}^\delta \cdot \nabla \vec{u}^\delta - \vec{g} \right) \right] \cdot \vec{v}^\delta \, \mathrm{d}\vec{x} + \int_\Omega \nabla p^\delta \cdot \vec{v}^\delta \, \mathrm{d}\vec{x} + 2\mu \int_\Omega \vec{\vec{S}}(\vec{u}^\delta) : \vec{\vec{S}}(\vec{v}^\delta) \mathrm{d}\vec{x} \\ &\quad + \sum_{j=1}^{N_p} \left(1 - \frac{\rho_{\mathrm{f}}}{\rho_j} \right) \left[M_j \left(\frac{\mathrm{d}\vec{V}_j}{\mathrm{d}t} - \vec{g} \right) \cdot \vec{Y}_j + \left(\vec{\vec{I}}_j \cdot \frac{\mathrm{d}\vec{\omega}_j}{\mathrm{d}t} + \vec{\omega}_j \times \vec{\vec{I}}_j \cdot \vec{\omega}_j \right) \cdot \vec{\Theta}_j \right] \\ &\quad = \sum_{j=1}^{N_p} \langle \vec{\lambda}_j^\delta, \vec{v}^\delta - \vec{Y}_j - \vec{\Theta}_j \times (\vec{x} - \vec{G}_j) \rangle_j + 2\mu \int_{\partial\Omega_{\mathrm{N}}} \vec{n} \cdot \vec{\vec{S}}(\vec{u}^\delta) \cdot \vec{v}^\delta \, \mathrm{d}s \quad \forall \vec{v}^\delta \in V^\delta, \ \ \forall \vec{Y}_j \in \mathbb{R}^3, \ \ \forall \vec{\Theta}_j \in \mathbb{R}^3, \end{aligned} \tag{7}$$

$$\int_\Omega q^\delta \nabla \cdot \vec{u}^\delta \, \mathrm{d}\vec{x} = 0, \quad \forall q^\delta \in V^\delta, \tag{8}$$

$$\left\langle \vec{\mu}_j^\delta, \frac{\partial \vec{\lambda}_j^\delta}{\partial t} + \tau(\vec{u}^\delta - \vec{V}_j - \vec{\omega}_j \times (\vec{x} - \vec{G}_j)) \right\rangle_j = 0, \quad \forall \vec{\mu}_j^\delta \in \Lambda_j^\delta, \ \ \forall j = 1, \ldots, N_p, \tag{9}$$

$$\frac{\mathrm{d}\vec{G}_j}{\mathrm{d}t} = \vec{V}_j, \quad \forall j = 1, \ldots, N_p. \tag{10}$$

For time integration we employ a stiffly-stable velocity-correction projection scheme [19]. For Navier–Stokes equations this scheme propagates the fields $\vec{u}^n$, p^n, $\vec{V}_j^n$, $\vec{\omega}_j^n$, $\vec{G}_j^n$, $\vec{\lambda}_j^n$, $\forall j = 1, \ldots, N_p$, over a time step Δt to determine the fields $\vec{u}^{n+1}$, p^{n+1}, $\vec{V}_j^{n+1}$, $\vec{\omega}_j^{n+1}$, $\vec{G}_j^{n+1}$, $\vec{\lambda}_j^{n+1}$, $\forall j = 1, \ldots, N_p$ in the following four substeps.

2.1. Non-linear term

Compute $\hat{u}$ via the solution of

$$\rho_f \int_\Omega \frac{\hat{u} - 2\vec{u}^n + \frac{1}{2}\vec{u}^{n-1}}{\Delta t} \cdot \vec{v}\,\mathrm{d}\vec{x} = \rho_f \int_\Omega [(2\vec{N}(\vec{u}^n) - \vec{N}(\vec{u}^{n-1})) + (2\vec{g}^n - \vec{g}^{n-1})] \cdot \vec{v}\,\mathrm{d}\vec{x}, \tag{11}$$

where $\vec{N}(\vec{u})$ is the non-linear term in convective form, $\vec{N}(\vec{u}) = -\vec{u} \cdot \nabla\vec{u}$.

2.2. Particle solve

We assume circular rigid particles hereafter and thus omit the non-linear term $\vec{\omega} \times \vec{\vec{I}} \cdot \vec{\omega}$ in the particle angular velocity equation. Let $F_j^n(\vec{Y}_j) = \langle \vec{\lambda}_j, \vec{Y}_j \rangle_j^n$ and $T_j^n(\vec{\Theta}_j) = \langle \vec{\lambda}_j^n, \vec{\Theta}_j \times (\vec{x} - \vec{G}_j^n) \rangle_j$. We compute the particle position, and the translational and angular velocities using the second-order Adams–Bashforth scheme:

$$\vec{G}_j^{n+1} = \vec{G}_j^n + \frac{\Delta t}{2}(3\vec{V}_j^n - \vec{V}_j^{n-1}), \quad \forall j = 1, \ldots, N_p, \tag{12}$$

$$\left(1 - \frac{\rho_f}{\rho_j}\right) M_j \frac{\vec{V}_j^{n+1} - \vec{V}_j^n}{\Delta t} \cdot \vec{Y}_j = \left(1 - \frac{\rho_f}{\rho_j}\right) M_j \vec{g} \cdot \vec{Y}_j - \frac{1}{2}[3F_j^n(\vec{Y}_j) - F_j^{n-1}(\vec{Y}_j)], \quad \forall j = 1, \ldots, N_p, \tag{13}$$

$$\left(1 - \frac{\rho_f}{\rho_j}\right) \vec{\vec{I}}_j \cdot \frac{\vec{\omega}_j^{n+1} - \vec{\omega}_j^n}{\Delta t} \cdot \vec{\Theta}_j = \frac{1}{2}[3T_j^n(\vec{\Theta}_j) - T_j^{n-1}(\vec{\Theta}_j)], \quad \forall j = 1, \ldots, N_p. \tag{14}$$

2.3. Pressure solve

We compute p^{n+1} and $\hat{\hat{u}}$ via the solution of

$$\rho_f \int_\Omega \frac{\nabla \cdot \hat{\hat{u}} - \nabla \cdot \hat{u}}{\Delta t} \Phi\,\mathrm{d}\vec{x} = \int_\Omega \nabla p^{n+1} \cdot \nabla\Phi\,\mathrm{d}\vec{x} - \int_{\partial\Omega} \frac{\partial p^{n+1}}{\partial n} \Phi\,\mathrm{d}s, \quad \forall \Phi \in V^\delta, \tag{15}$$

$$\int_\Omega q \nabla \cdot \vec{u}^{n+1}\,\mathrm{d}\vec{x} = 0, \quad \forall q \in V^\delta. \tag{16}$$

In the above equations the pressure boundary condition is (see [19,20])

$$\frac{\partial p^{n+1}}{\partial n} = \vec{n} \cdot [(2\vec{N}(\vec{u}^n) - \vec{N}(\vec{u}^{n-1})) - \nu(2\nabla \times \vec{\omega}^n - \nabla \times \vec{\omega}^{n-1}) + (2\vec{g}^n - \vec{g}^{n-1})],$$

where $\vec{\omega}$ is the vorticity.

2.4. Viscous effect and rigid-body motion constraint

We compute $\vec{u}^{n+1}$ and $\vec{\lambda}_j^{n+1}$ with a sub-cycling procedure. Let $\vec{\lambda}_j^{n+1,0} = 0$. For $k = 1, \ldots, K$, compute $\vec{u}^{n+1}$ and $\vec{\lambda}_j^{n+1,k}$ via the solution of

$$\rho_{\mathrm{f}} \int_{\Omega} \frac{\frac{3}{2}\vec{u}^{n+1} - \hat{\hat{u}}}{\Delta t} \cdot \vec{v}\,\mathrm{d}\vec{x} + 2\mu \int_{\Omega} \vec{\vec{S}}(\vec{u}^{n+1}) : \vec{\vec{S}}(\vec{v})\mathrm{d}\vec{x} = \sum_{j=1}^{N_p} \langle \vec{\lambda}_j^{n+1,k}, \vec{v} \rangle_j + 2\mu \int_{\partial\Omega_{\mathrm{N}}} \vec{n} \cdot \vec{\vec{S}}(\vec{u}^{n+1}) \cdot \vec{v}\,\mathrm{d}\vec{x}, \tag{17}$$

$$\left\langle \mu_j, \frac{\vec{\lambda}_j^{n+1,k} - \vec{\lambda}_j^{n+1,k-1}}{\Delta t/K} + \tau(\vec{u}^{n+1} - \vec{V}_j^{n+1} - \vec{\omega}_j^{n+1} \times (\vec{x} - \vec{G}_j^{n+1})) \right\rangle_j = 0, \quad \forall \vec{\mu}_j \in \Lambda_j^{\delta}. \tag{18}$$

The penalty parameter τ is chosen such that the norm of $(\vec{u}^{n+1} - \vec{V}_j^{n+1} - \vec{\omega}_j^{n+1} \times (\vec{x} - \vec{G}_j^{n+1}))$, $\forall j = 1, \ldots, N_p$ is minimized, and the value is in the range of 10^3–10^4. In the above equations, step 2.3 and step 2.4 are coupled because $\nabla \cdot \hat{\hat{u}} \neq 0$ due to the Lagrange multiplier, unlike the standard splitting scheme [19]. This coupling is handled with an outer-level iteration in the implementation. For the results reported in Section 4 two iterations are typically used at the outer level (between step 2.3 and step 2.4).

The Lagrange multiplier $\vec{\lambda}$ plays the role of a source term (see Eq. (1)). In the original velocity-correction projection scheme [19], the source term is handled together with the non-linear term in step 2.1. However, we found through systematic numerical experiments that handling the Lagrange multipliers in the non-linear step instead of as in the current scheme produces larger errors. In Fig. 1 we compare the streamwise velocity profiles for the flow (finite Reynolds number) past a circular cylinder in the center of a 2D channel from DNS: the current DLM scheme and another scheme, in which the Lagrange multiplier is handled in the non-linear step. The channel dimension is 2×2 ($-1 \leqslant x \leqslant 1$, $-1 \leqslant y \leqslant 1$), and the cylinder diameter is $2R = 1$. The density and the viscosity of the fluid are $\rho_{\mathrm{f}} = 1.0$ and $v = 1.0$, respectively. The flow is driven by a force $F_x = 2$ in the streamwise direction. The simulations were conducted on a 64×64 grid for both

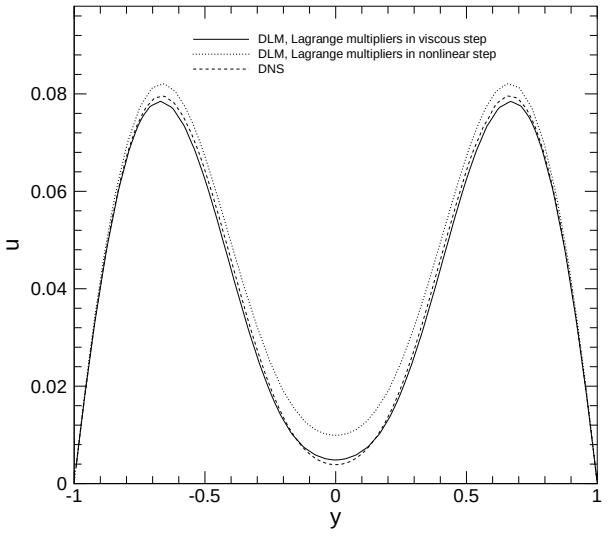

Fig. 1. Comparison of DNS with two DLM schemes: (1) Lagrange multiplier is handled in viscous step (current scheme); and (2) Lagrange multiplier is handled in non-linear step. Shown are streamwise velocity profiles at $x = 0.6$ for the flow past a circular cylinder (radius 0.5) at the center of a 2D channel (dimension 2×2).

DLM schemes. The current scheme results in much smaller discrepancies compared to DNS. In contrast, large errors in the velocity profiles are observed when the Lagrange multiplier term is treated in the non-linear step.

3. Review of force coupling method and DNS

We present here a short summary of the FCM [23,27] for simulating particle dynamics in liquid flows. The method is based on representing the particles by force multipoles distributed over a finite volume. Consider the incompressible Navier–Stokes equations

$$\rho_{\mathrm{f}}\frac{\mathrm{D}\vec{u}}{\mathrm{D}t} = -\nabla p + \mu\nabla^2\vec{u} + \vec{f}(\vec{x},t), \tag{19}$$

$$\nabla\cdot\vec{u} = 0, \tag{20}$$

where ρ_{f}, p, $\vec{u}$ and μ are the fluid density, pressure, velocity and viscosity, respectively. The term $\vec{f}(\vec{x},t)$ denotes the total effect of *two-way coupling* forces on the flow from each spherical particle n centered at $\vec{Y}^n(t)$:

$$f_i^n(\vec{x},t) = F_i^n\Delta(\vec{x}-\vec{Y}^n(t)) + G_{ij}^n\frac{\partial}{\partial x_j}\Delta'(\vec{x}-\vec{Y}^n(t)), \quad i=1,2,3, \ \ \forall n=1,\ldots,N_p, \tag{21}$$

where N_p is the number of particles. In the above equation both $\Delta(\vec{x})$ and $\Delta'(\vec{x})$ are Gaussian distribution functions of the form

$$\Delta(\vec{x}) = (2\pi\sigma^2)^{-3/2}\exp(-\vec{x}^2/(2\sigma^2)).$$

The values of the length scales σ and σ' are directly related to the particle radius R with $R/\sigma=\sqrt{\pi}$ and $R/\sigma' = (6\sqrt{\pi})^{1/3}$ as calculated in [23,27]. The first term in Eq. (21) represents a force monopole of strength $\vec{F}$ while the second term represents a force dipole of strength G_{ij}. The monopole strength is set by the total external forces. For non-deformable particles, the force dipole is calculated iteratively through the minimization of the integral-averaged strain rate in the volume occupied by the particles. The particle velocity $\vec{V}_{\mathrm{p}}(t)$ is evaluated from a volume integral of the local fluid velocity inside the particle region as

$$\vec{V}_{\mathrm{p}}(t) = \int_{\Omega_{\mathrm{p}}}\vec{u}(\vec{x},t)\Delta(\vec{x}-\vec{Y}(t))\mathrm{d}\Omega_{\mathrm{p}},$$

where Ω_{p} is the volume of the particle.

The DLM simulations are systematically compared against direct numerical simulations performed with the *Nektar* code [21] in the following sections. The *Nektar* code implements the spectral/*hp* element method [20] for incompressible and compressible unsteady flows in general 3D geometries. Flow variables are represented in terms of Jacobi polynomial expansions. It is efficient for handling flows in complex geometries while the spectral representation within each element provides high-order accuracy.

4. Results and discussion

We test and compare the spectral DLM method with DNS and FCM for several 2D and 3D benchmark flow problems for Stokes flow as well as finite Reynolds number flows. The comparison with FCM is conducted only for 3D flows.

4.1. Effect of collocation point distribution

The "collocation" points on which to enforce the rigid-body motion can be distributed by different means inside the particle regions. We investigate three different distributions (Fig. 3) for the flow past a circular cylinder in a 2D channel (Fig. 2) at a finite Reynolds number. The length and the height of the channel are chosen to be 2 ($-1 < x < 1$, $-1 < y < 1$), and the cylinder is placed at the center of the channel with a radius $R = 0.25$. In the first configuration (regular), the collocation points are distributed on nine concentric circles; the points are uniformly distributed on each circle. The outer-most circle coincides with the boundary of the cylinder. In the second configuration (random), the collocation points are distributed randomly inside the cylinder region. In the third configuration (hybrid), the underlying flow grid points inside the cylinder, along with the intersection points between the cylinder boundary and the grid lines, are chosen as the collocation points.

This flow will be discussed in more detail in Section 4.4. Fig. 3 shows the streamwise velocity (left) and wall-normal velocity (right) profiles of the flow for the three collocation point distributions, along with the DNS results. This finite Reynolds number flow is driven by a force ($F_x = 20$), with periodic boundary conditions in the streamwise direction. The same number of collocation points is used for all three distributions. The regular distribution and hybrid distribution yield almost identical velocity values; both results agree with DNS very well. The random distribution yields velocities close to the other cases, but a slight asymmetry in the profiles is observed.

4.2. Convergence rate

Next, we examine the convergence rate of the spectral DLM method with a 2D analytic flow field expressed by

$$u = e^{2\pi y}\cos 2\pi x,$$

$$v = e^{2\pi y}\sin 2\pi x,$$

$$p = -\tfrac{1}{2}e^{4\pi y}, \quad 0 \leqslant x \leqslant 2, \ -1 \leqslant y \leqslant 1,$$

on a rectangular flow domain, where u and v are the x and y components of the velocity and p is the pressure. Velocity values calculated based on the analytic expression are used to impose the Dirichlet

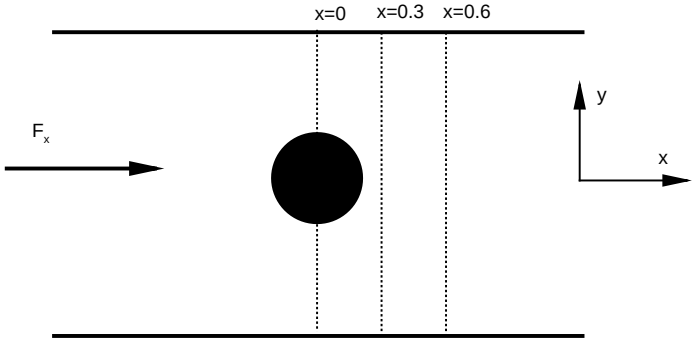

Fig. 2. Schematic for flow past a circular cylinder in a 2D channel.

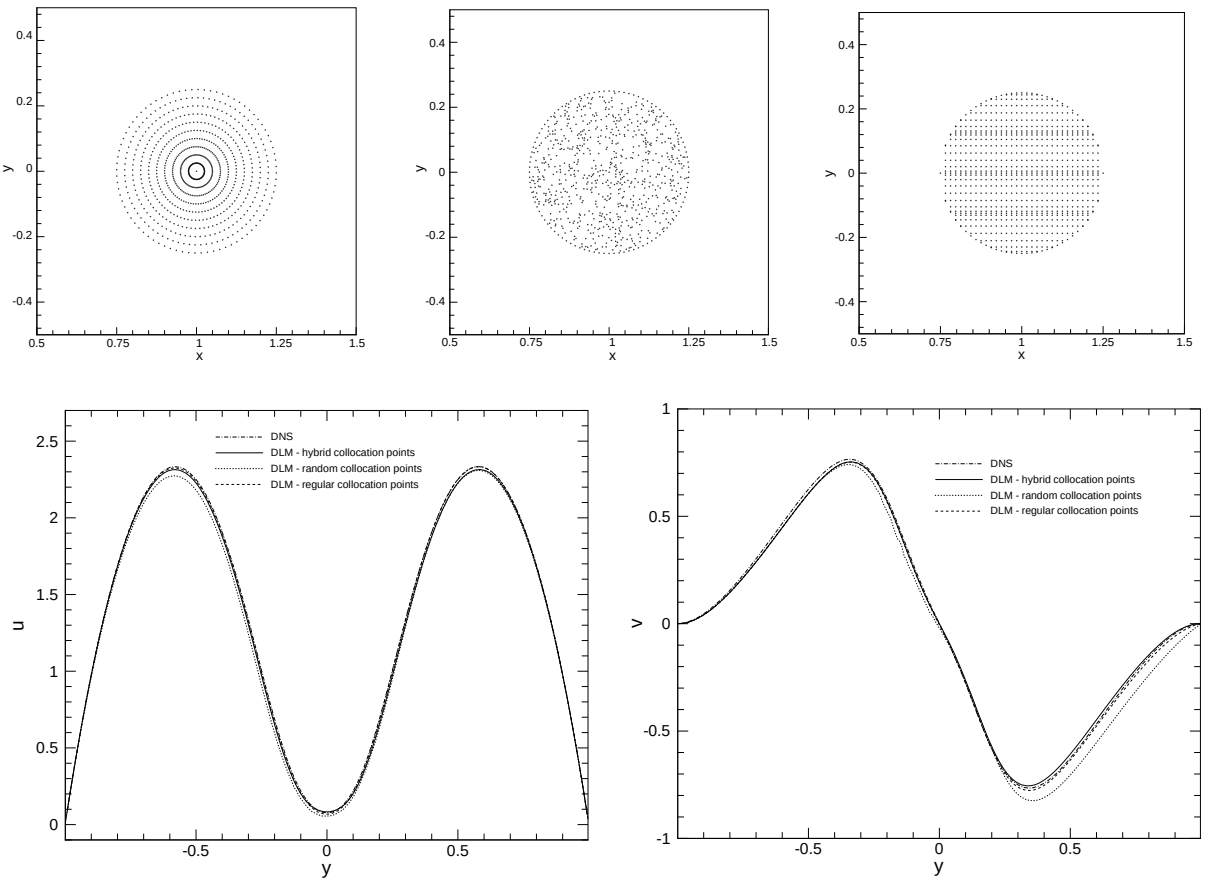

Fig. 3. Effect of collocation point distribution in flow past a 2D circular cylinder. Top row: three distributions of collocation points: regular distribution (left), random distribution (middle), hybrid distribution (right). Bottom row: streamwise (left) and wall-normal (right) velocity profiles at $x = 0.3$ in cylinder wake for the three distributions and DNS.

boundary conditions at $y = -1$ and $y = 1$. In the x-direction periodic boundary conditions are imposed at $x = 0$ and $x = 2$. In addition, we impose the constraint that the velocity satisfies the analytic expression through DLMs in a region at the center of the flow domain. Two cases are considered. In the first case the constraint is imposed on a square region ($0.9325 \leqslant x \leqslant 1.0625$ and $-0.0625 \leqslant y \leqslant 0.0625$). In the second case the constraint is imposed on a circular disk region with radius $R_{\text{disk}} = 0.125$. For the square region no interpolation is needed on the boundary collocation points while for the disk region the velocities need to be interpolated at the collocation points on the disk boundary.

The Navier–Stokes equations are solved with a Fourier spectral expansion in the x-direction and a spectral element expansion in the y-direction. For the case of a square region we place 32 grid points in the x-direction and 32 equal-sized spectral elements in the y-direction. As a result, there are three grid points in x-direction and two spectral elements in y-direction in the central square region where the DLMs are employed to enforce the constraint. For the case of a disk region, we place 64 grid points in the x-direction and 16 equal-sized spectral elements in y-direction. As a result, there are 9 grid points in x-direction and two spectral elements in y-direction in the diameter of the circular disk where DLMs are employed to enforce the constraint (note that we have chosen a larger disk region and a larger grid in

order to better resolve the circular boundary). The flow starts from rest and evolves to steady state. We then calculate the L^2 and L^∞ errors of the computed flow velocities relative to the analytic solution. In Fig. 4 we plot these errors of the x velocity component versus the order of the expansion polynomials for both cases. The numerical errors decrease exponentially as the spectral order increases, indicating that the spectral DLM method indeed achieves *spectral accuracy* for this particular example.

4.3. Flow past a 2D spinning cylinder near a moving wall

We consider a 2D Stokes flow past a circular cylinder spinning counter-clockwise near a wall that moves in the streamwise direction; this flow is known as the Wannier flow [20]. An exact solution exists for this flow in the Stokes regime, which depends only on cylinder radius, R, its rate of rotation, ω, the distance between the center of the cylinder to the moving wall, d, and the velocity of the wall, U. If we place the origin of the coordinate system at the center of the cylinder, the exact solution is given by the following expressions:

$$u = U - 2(a_1 + a_0 Y_1)\left[\frac{s + Y_1}{K_1} + \frac{s - Y_1}{K_2}\right] - a_0 \ln\frac{K_1}{K_2} - \frac{a_2}{K_1}\left[s + Y_2 - \frac{(s + Y_1)^2 Y_2}{K_1}\right] - \frac{a_3}{K_2}\left[s - Y_2 + \frac{(s - Y_1)^2 Y_2}{K_2}\right], \tag{22}$$

$$v = \frac{2x}{K_1 K_2}(a_1 + a_0 Y_1)(K_2 - K_1) - \frac{x a_2 (s + Y_1) Y_2}{K_1^2} - \frac{x a_3 (s - Y_1) Y_2}{K_2^2}, \tag{23}$$

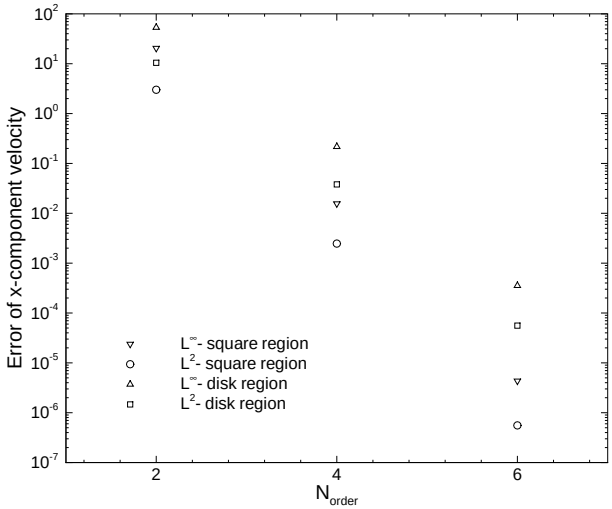

Fig. 4. Convergence rate of spectral element DLM method. N_{order} is the order of Jacobi polynomials in the spectral element discretization in y-direction.

where

$$s=\sqrt{d^2-R^2},\quad \Gamma=\frac{d+s}{d-s},\quad a_0=\frac{U}{\ln\Gamma},\quad a_1=-d\left(a_0+\frac{\omega R^2}{2s}\right),\quad a_2=2(d+s)\left(a_0+\frac{\omega R^2}{2s}\right),$$
$$a_3=2(d-s)\left(a_0+\frac{\omega R^2}{2s}\right),\quad Y_1=y+d,\quad Y_2=2Y_1,\quad K_1=x^2+(s+Y_1)^2,\quad K_2=x^2+(s-Y_1)^2.$$

We compute this flow with the spectral DLM method, enforcing the rotation of the cylinder with DLMs. Fig. 6 shows a comparison of the streamwise and wall-normal velocity profiles between the computed result and the exact solution at three streamwise locations (indicated by the dashed lines in Fig. 5): $x=0$, $x=R$ and $x=2R$. The parameters are chosen as $U=1.0$, $\omega=2.0$, $R=0.25$, and $d=2.5$. The numerical results match the exact solution quite well, with slight discrepancies at locations near the cylinder. These discrepancies are due to the mismatch of the boundary conditions in the streamwise direction between the exact and the numerical solution. Specifically, Eqs. (22) and (23) express a flow solution in a half-infinite domain. However, in the simulation Dirichlet boundary conditions are applied in the wall-normal direction. In the streamwise direction we employ Fourier spectral expansions, and thus a periodic condition is implicitly assumed. Although we choose a very large flow domain in the streamwise direction ($50R$) in the computations, the effect of the periodic boundary condition can still be observed near the cylinder in the Stokes regime.

4.4. Flow past a circular cylinder in a 2D channel

We return now to the flow past a circular cylinder in a 2D channel (Fig. 2) and consider three finite Reynolds numbers as well as the Stokes flow. The dimension of the channel is chosen as: $-1\leqslant x\leqslant 1$, $-1\leqslant y\leqslant 1$. The cylinder is placed at the center of the channel (the cylinder center is at $x=0, y=0$) with a radius $R=0.25$. Periodic boundary conditions are imposed at $x=-1$ and $x=1$. No-slip conditions are imposed on the channel walls at $y=-1$ and $y=1$. The density and viscosity of the fluid are chosen to be $\rho_f=1$ and $\nu=1$, respectively. A constant force F_x is applied to drive the flow in the x-direction. The Stokes case and three finite-Reynolds-number cases are calculated with different driving forces. Table 1 summarizes the parameters in these simulations.

In the spectral DLM computations, a Fourier spectral expansion is used in the x-direction and a spectral element expansion is used in the y-direction. DLMs are used to enforce the zero-velocity constraint in the cylinder region. We choose the "hybrid" distribution of the collocation points. They consist of all the flow

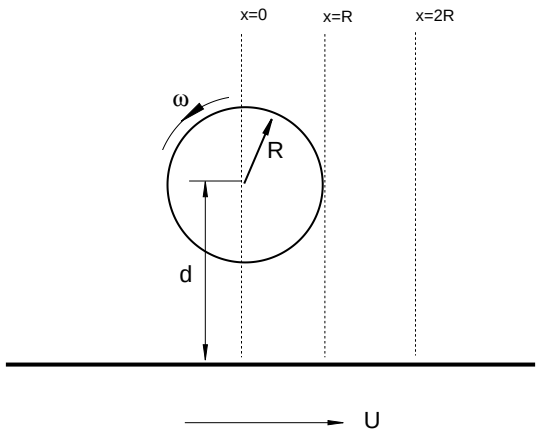

Fig. 5. Sketch of the flow past a spinning cylinder near a moving wall.

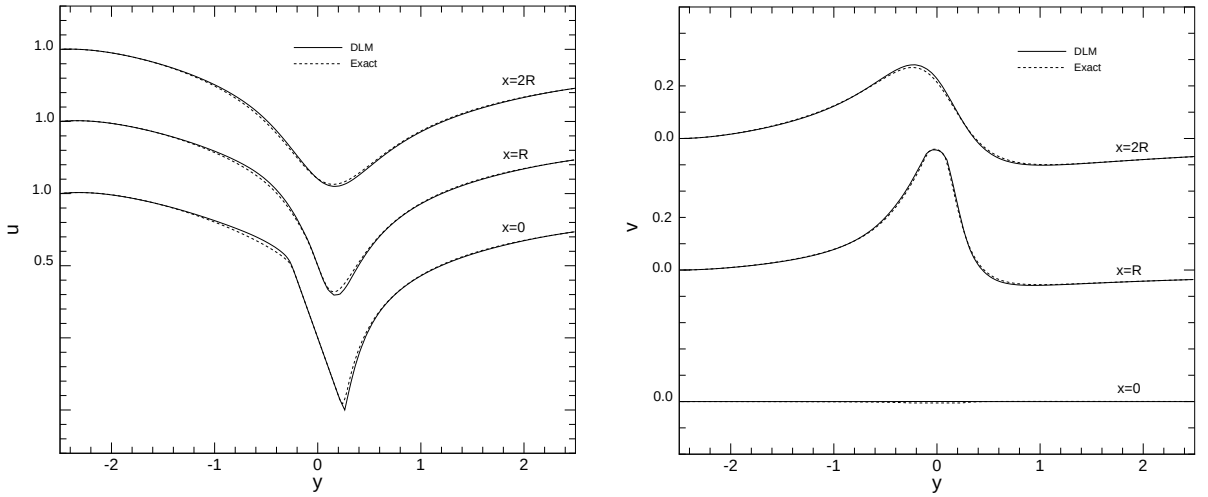

Fig. 6. Comparison of velocity profiles between computed results and the exact solution for the Wannier flow. Left: streamwise velocity. Right: wall-normal velocity. Because the line $x = 0$ intersects the cylinder, a portion of a straight line is observed in the streamwise velocity profile at this location.

Table 1
Force parameters for the flows past a circular cylinder in a 2D channel

	Case S1	Case F1	Case F2	Case F3
Re_F	2.0	2.0	20.0	100.0

Case S1: Stokes flow. Case F1–F3: finite Reynolds-number flows. Re_F is the Reynolds number based on the force, $Re_F = \frac{F_x}{\mu\nu}$, where F_x is a force driving the flow.

quadrature points lying inside the cylinder region and the intersection points between the cylinder boundary and the vertical grid lines. The flow velocities on the boundary collocation points are obtained with a spectral element interpolation procedure

$$u(y) = \sum_{p=1}^{N_m} u_p \phi_p(y), \tag{24}$$

where y is the point where the velocity u is to be interpolated, u_p are modes in the transform space, $\phi_p(y)$ are basis functions (Jacobi polynomials of order p) evaluated at point y.

In Figs. 7 and 8 we compare the streamwise velocity profiles (left column) and wall-normal velocity profiles (right column) at three streamwise locations, $x = 0.0, 0.3, 0.6$, between the spectral DLM and the direct numerical simulation results. The latter were obtained with the spectral element code *Nektar*, for the four cases simulated. This code uses Jacobi polynomials with mixed weights on triangular or tetrahedra elements [20]. For all four cases with the spectral DLM method a grid of 128×128 is used that produces the converged results. The spectral DLM method and DNS produce the same distributions with almost identical values in magnitude. At the highest Reynolds number, $Re_F = 100$, there are some differences in the wall-normal velocity values between spectral DLM and DNS in the region outside of the cylinder wake.

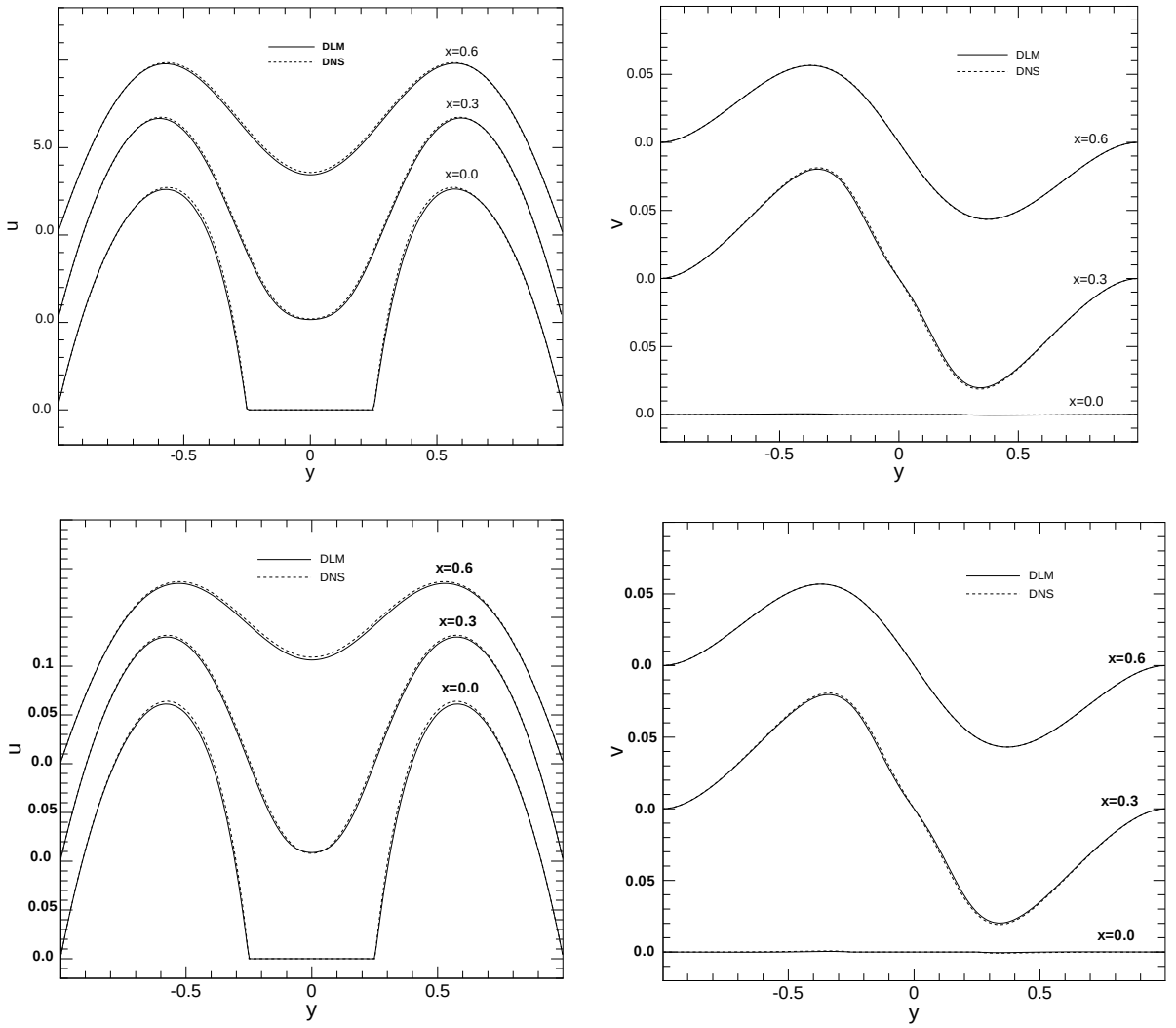

Fig. 7. Circular cylinder in 2D channel: comparison of velocity profiles between spectral DLM and DNS at three streamwise locations for the Stokes flow (top row) and finite Reynolds number (bottom row) flow, $Re_F = 2.0$. Left column: streamwise velocity. Right column: wall-normal velocity.

4.5. Flow past a square cylinder in a 2D channel

The next test case is the flow past a square cylinder in a 2D channel (Fig. 9). Unlike the circular cylinder case, there is no need for interpolation on the boundary "collocation" points for the square cylinder, which will give rise to more accurate results than with interpolations.

The channel dimension is identical to that in the circular cylinder case. The square cylinder covers a region, $-0.25 \leqslant x \leqslant 0.25$ and $-0.25 \leqslant y \leqslant 0.25$, at the center of the channel. Periodic conditions are imposed in the streamwise x-direction. No-slip conditions are applied in the wall-normal direction. The fluid density and viscosity are chosen to be $\rho_f = 1.0$ and $\nu = 1.0$, respectively.

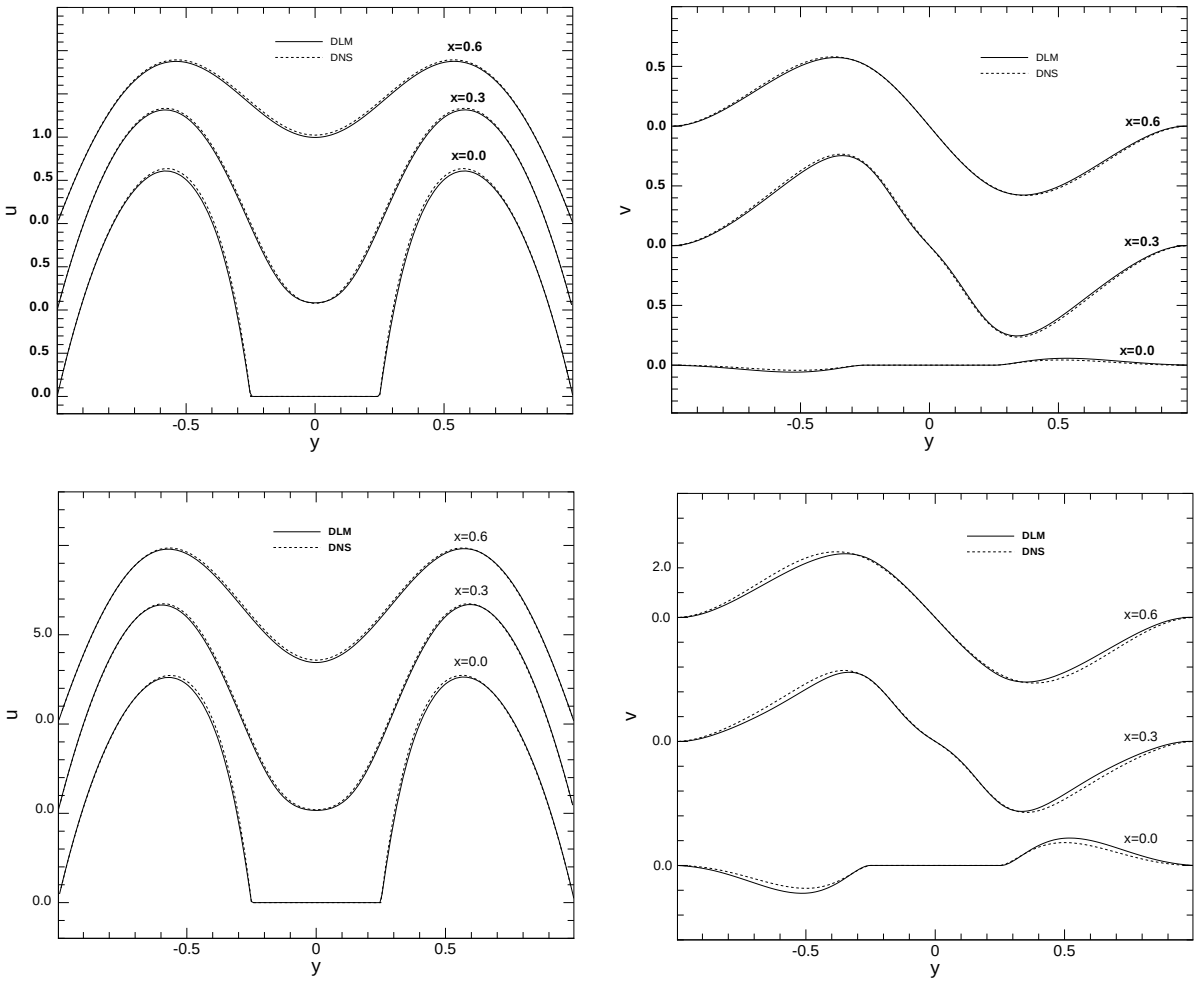

Fig. 8. Circular cylinder flow in 2D channel: comparison of velocity profiles between spectral DLM and DNS at three streamwise locations for flow past a circular cylinder at Reynolds numbers $Re_F = 20$ (top row) and $Re_F = 100$ (bottom row). Left column: streamwise velocity. Right column: wall-normal velocity.

The flow is driven by a constant force F_x in the streamwise x-direction. We compute four cases corresponding to different flow regimes and driving forces, with one case in the Stokes regime ($F_x = 2.0$) and three cases at finite Reynolds numbers ($F_x = 2.0, 20.0, 100.0$). The driving forces are chosen to be the same as those in the circular cylinder simulations as listed in Table 1.

Again, a Fourier spectral expansion is used in the x-direction and spectral element expansions are used in the y-direction in the spectral DLM method. DLMs are used to enforce the zero-velocity constraint in the square cylinder region. The "collocation" points on which the constraints are applied consist of the flow grid points lying within and on the boundary of the square cylinder. Because the boundary of the square cylinder coincides with the underlying grid lines, all the boundary "collocation" points are on the grid points of the flow. As a result, no interpolation is necessary in this case.

Figs. 10 and 11 show the comparison of the streamwise velocity (left column) and wall-normal velocity (right column) profiles between spectral DLM and DNS for three downstream locations, $x = 0.0, 0.3, 0.6$. With the spectral DLM all four cases are computed on a grid 128×128 which gives the converged results.

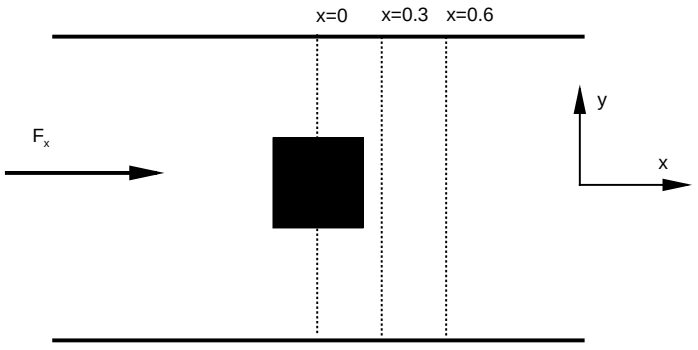

Fig. 9. Schematic of flow past a square cylinder in a 2D channel.

Spectral DLM method and DNS produce identical distributions and velocity magnitudes for the Stokes case and the two lower Reynolds numbers $Re_F = 2$ and 20. At the highest Reynolds number $Re_F = 100$, the spectral DLM method and DNS produce identical results for the streamwise velocity. Slight discrepancies exist in the wall-normal velocity magnitude in the region outside the wake of the square cylinder. The comparisons in this section as well as the previous section indicate that the boundary "collocation" points used in interpolating fields in the DLM method have a notable effect on the accuracy of the results.

4.6. Flow past a sphere in center of a 3D channel

Next we test the spectral DLM method for flow past a sphere placed at the center of a 3D channel at a finite Reynolds number (Fig. 12), and compare these results with DNS and FCM results.

The 3D channel dimension is $30 \times 10 \times 30$ ($-15 \leqslant x \leqslant 15$, $-5 \leqslant y \leqslant 5$, $-15 \leqslant z \leqslant 15$). A sphere with radius $R = 1.0$ is placed at the center of the channel; the sphere center coincides with the origin of the coordinate system. The two walls of the channel ($y = -5$ and $y = 5$) move at a constant speed $U = 0.78$ in the x-direction, which drives the flow inside the channel. The fluid density and viscosity are chosen to be $\rho_f = 1.0$ and $v = 1.0$, respectively. The Reynolds number based on the wall velocity and the particle diameter is 1.56. Periodic boundary conditions are applied in both the x- and z-directions. No-slip boundary conditions are imposed on the two channel walls.

This flow is computed with three methods: DLM, DNS and FCM. With the DLM method, we employ Fourier expansions in both x- and z-directions and spectral element expansions in the y-direction to discretize the Navier–Stokes equations. DLMs are used to impose the zero-flow constraints in the region occupied by the sphere. The constraints are applied at all the flow grid points inside the sphere and at the boundary "collocation" points consisting of the intersection points between the vertical grid lines and the sphere surface. We employ the spectral element interpolation procedure (Eq. (24)) to interpolate the velocities on the boundary "collocation" points when solving the Lagrange multipliers.

The FCM calculation of the flow is conducted in a fashion slightly different than the DNS and the spectral DLM method. We first conduct the DNS of this flow, and compute the force on the sphere. This force is then used as the force monopole strength in the x-direction for the FCM simulations. In the FCM simulations the channel walls are fixed in space. Periodic conditions are imposed in x- and z-directions, and no-slip conditions are applied on the channel walls. The sphere is positioned at the centerline and initially at rest. Subsequently, the sphere is released and falls along the centerline under the influence of the force monopole. After the sphere reaches the terminal velocity, the velocity field surrounding the sphere is transformed into the laboratory reference frame and compared with the DNS and spectral DLM results.

In Fig. 13 we compare the velocity profiles at three streamwise locations, $x = 0$, R and $2R$ in the center plane ($z = 0$), computed with all three methods. The left plot shows the streamwise velocity (x-component)

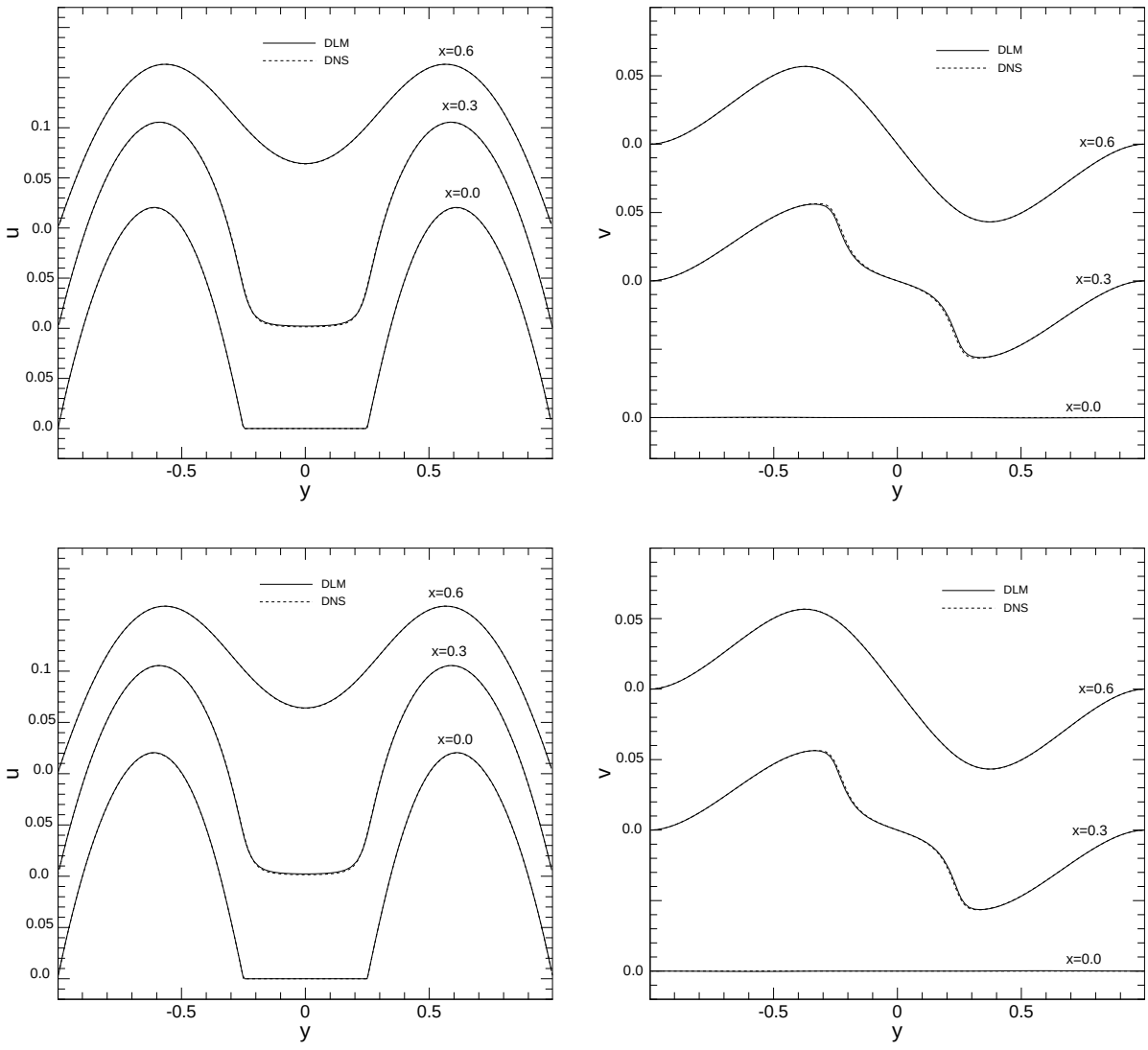

Fig. 10. Square cylinder in 2D channel: comparison of velocity profiles between spectral DLM and DNS at three streamwise locations for Stokes flow (top row) and a finite Reynolds number (bottom row) flow, $Re_F = 2.0$. Left column: streamwise velocity. Right column: wall-normal velocity.

and the right one shows the wall-normal velocity (y-component). The spanwise velocity is not shown because it is zero in the center plane with all three methods. All three methods agree in the far field $x = 2R$. Near the sphere, $x = 0$ and R, the spectral DLM demonstrates a good agreement with DNS; larger discrepancies are observed between FCM and DNS in this region.

4.7. Flow past a sphere near one wall of a 3D channel

The last test case is the flow past a sphere located near one wall of a 3D channel, which has a length 15, a height 7 and a width 7. The origin of the coordinate system is located at the center of the channel so that the

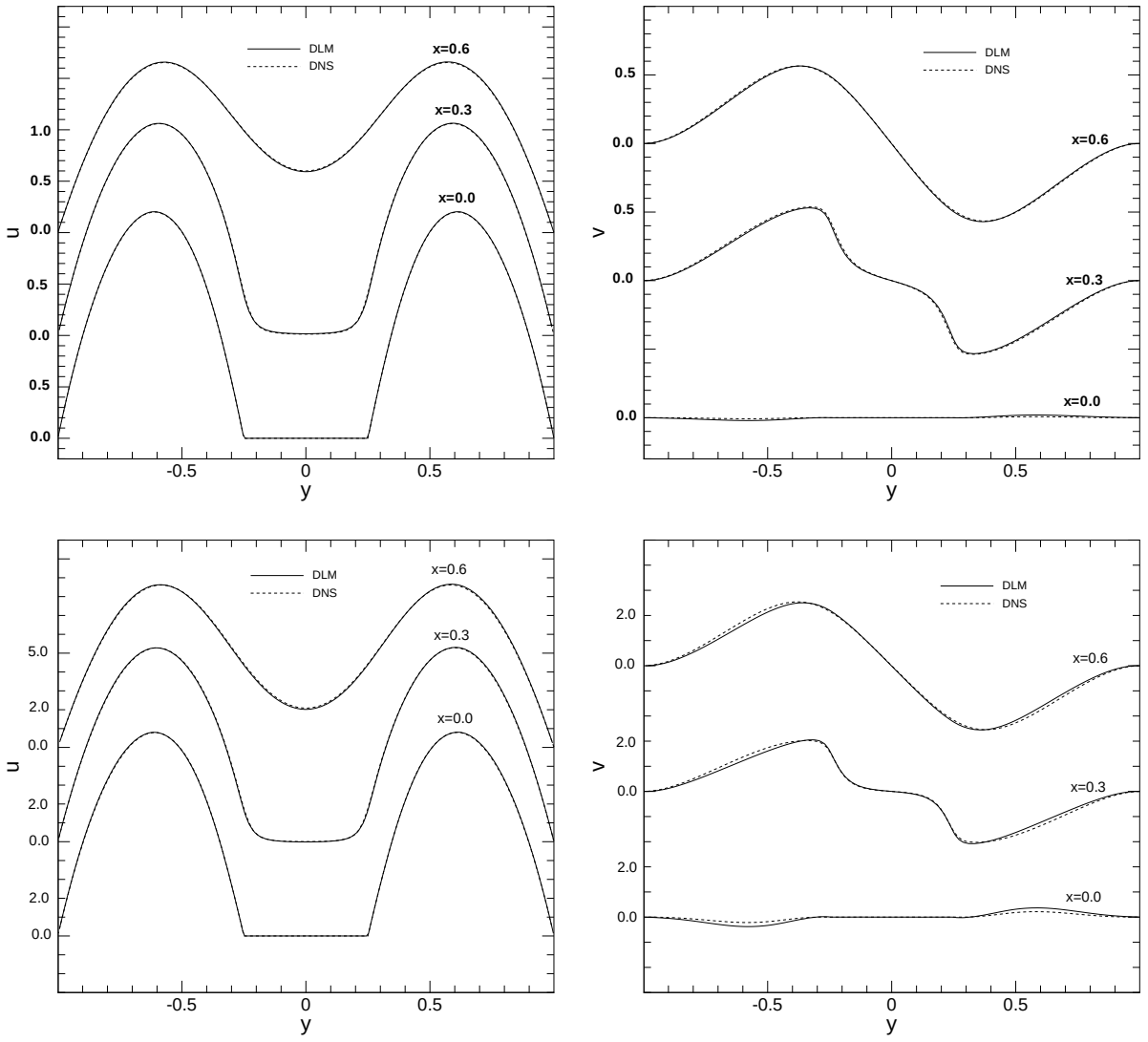

Fig. 11. Square cylinder in a 2D channel: comparison of velocity profiles between spectral DLM and DNS at three streamwise locations at Reynolds numbers $Re_F = 20$ (top row) and $Re_F = 100$ (bottom row). Left column: streamwise velocity. Right column: wall-normal velocity.

flow domain covers $-7.5 \leqslant x \leqslant 7.5$, $-3.5 \leqslant y \leqslant 3.5$ and $-3.5 \leqslant z \leqslant 3.5$. A sphere of radius $R = 1$ is placed near the lower channel wall with its center at $(x_0, y_0, z_0) = (0, -1.5, 0)$. The fluid density and viscosity are chosen to be $\rho_f = 1.0$ and $\nu = 1.0$, respectively. Periodic conditions are imposed in x- and z-directions, and no-slip conditions are applied on the two walls of the channel. The flow is driven by a constant force in the x-direction, $F = \frac{2\nu}{h^2}$, where h is the channel half width.

The spectral DLM simulations employ Fourier expansions in x- and z-directions and a spectral element discretization in y-direction. DLMs are used to impose the zero-flow constraint inside the sphere. The "collocation points" consist of the flow grid points lying inside the sphere and intersection points between the surface of the sphere and the underlying flow grid lines. On the boundary collocation points the flow

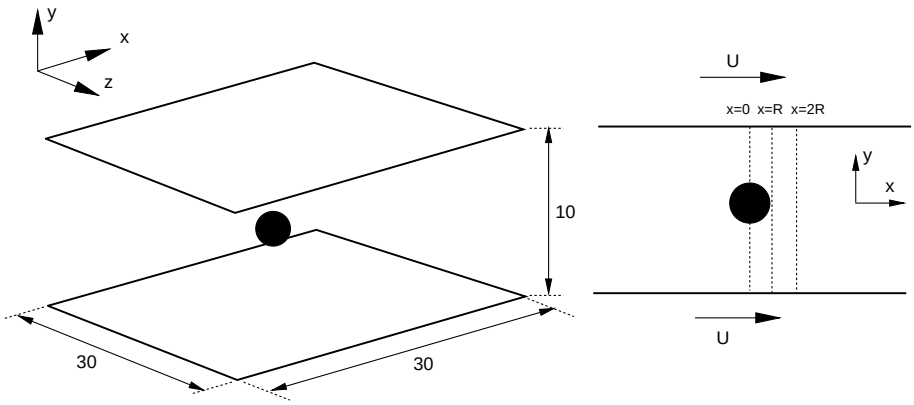

Fig. 12. Schematic of a sphere in the center of a 3D channel. The dimensions of the channel are listed in the figure. The two walls move in the x-direction. Dashed lines mark the locations of the velocity profiles to be compared.

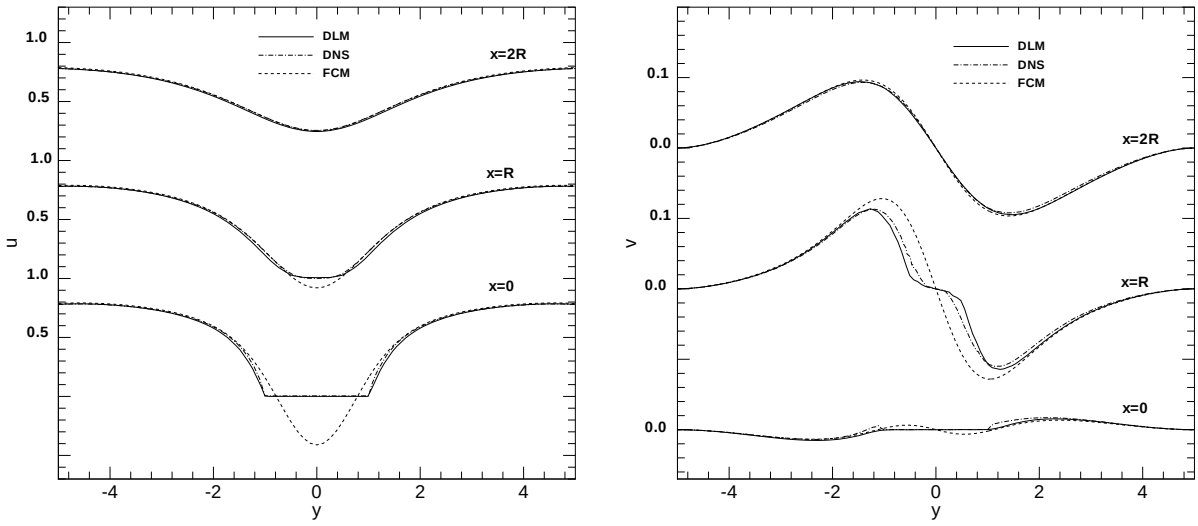

Fig. 13. Sphere at center: comparison of velocity profiles between spectral DLM, DNS and FCM at three streamwise locations at Reynolds number $Re = 1.56$ (based on wall moving velocity and sphere diameter). Left: streamwise velocity. Right: wall-normal velocity.

velocities are obtained via the spectral element interpolation procedure expressed by Eq. (24). In the FCM calculations a restoring force and torque are computed via a penalty method to keep the sphere from moving and rotating in the channel. The restoring force and torque are then used as the force monopole strength and dipole strength, respectively.

In Fig. 14 we plot the streamwise (left figure) and wall-normal (right figure) velocity profiles at three downstream locations, $x = 0$, R and $2R$, computed with all three methods. Similar to the observations in the previous section, all three methods agree with one another quite well in the region far away from the sphere ($x = 2R$). Closer to the sphere surface and inside the sphere, the spectral DLM results are in good agreement

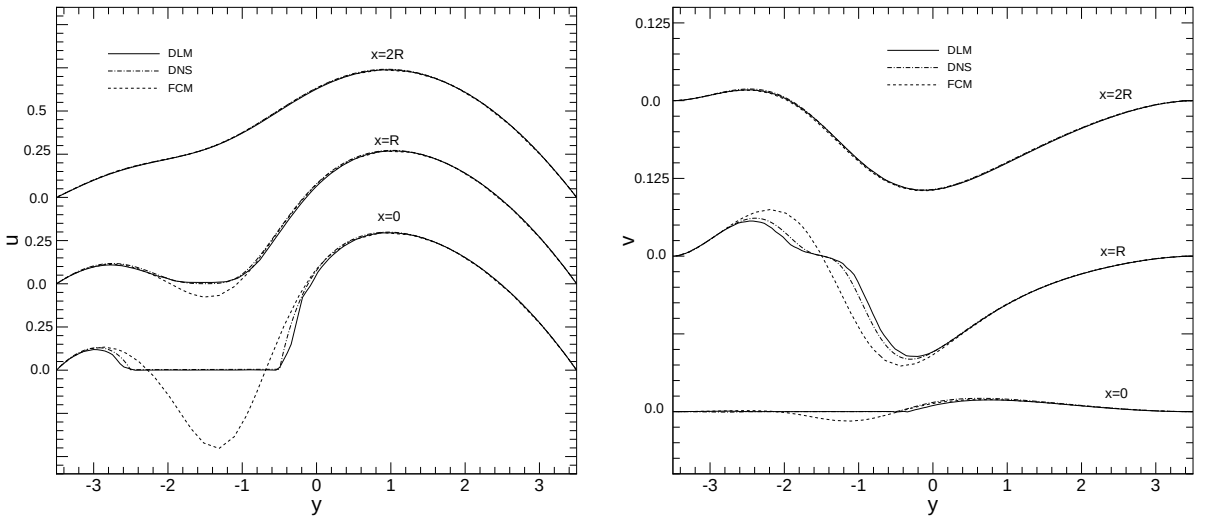

Fig. 14. Sphere off center: comparison of velocity profiles between spectral DLM, DNS and FCM at three streamwise locations at Reynolds number $Re = 1.55$ (based on the channel center line maximum velocity and sphere diameter). Left: streamwise velocity. Right: wall-normal velocity.

Table 2
Drag coefficient ($C_D = \text{drag}/\frac{1}{2}\rho_f U_m^2 d$, where U_m is the maximum velocity at the center line of the channel and d is the cylinder diameter), lift coefficient ($C_L = \text{lift}/\frac{1}{2}\rho_f U_m^2 d$), and the torque coefficient ($C_T = \text{torque}/\frac{1}{4}\rho_f U_m^2 d^2$) on the sphere near one wall in a 3D channel

	Elements/grid	C_D	C_L	C_T
DNS	4608 (5th order)	33.932	1.236	5.064
	4608 (7th order)	33.929	1.236	5.066
	4608 (8th order)	33.929	1.236	5.066
FCM	360 (4th order)	35.122	1.274	4.872
	360 (6th order)	35.175	1.274	5.251
	360 (8th order)	35.306	1.276	5.251
DLM	$96 \times 60 \times 96$	33.475	1.172	5.236
	$96 \times 72 \times 96$	33.533	1.211	5.157
	$96 \times 84 \times 96$	33.724	1.210	5.175

with DNS results, while larger discrepancies between FCM and DNS results are observed in these regions. Due to asymmetry in the configuration, the flow exerts a torque and a lift force on the sphere. The coefficients for the drag and lift forces on the sphere and the torque with respect to z-axis computed with all three methods are summarized in Table 2. FCM over-predicts the drag force on the sphere. However, given the small number of elements, FCM simulations have produced lift and torque values that are in quite good agreement with DNS. The drag and lift forces produced by spectral DLM are in good agreement with DNS results; the errors are within 2%. It is noted that poorly resolved regions on the surface of the sphere could affect the accuracy of the torque in DLM. For example, if the boundary collocation points consist only of intersection points between the sphere surface and the vertical grid lines, the torque will be over-predicted on the grid $96 \times 84 \times 96$ (with a value 5.37).

5. Summary

We have presented a method that extends the DLM formulation to spectral/spectral element discretizations for simulating particulate flows. We also compared this method with direct numerical simulation and the FCM for several 2D and 3D flow simulations covering the Stokes regime and finite Reynolds numbers. In all comparisons, the discretization method was spectral or spectral element so that the accuracy of DLM formulation can be tested within the same interpolation framework. The spectral DLM method that we developed implements the rigid-body motion of the particles via a penalty procedure.

In particular, the accuracy and convergence behavior of the method are quantified with an analytic flow field. The numerical errors decrease exponentially as the spectral order increases, indicating that the spectral DLM method achieves spectral accuracy. This result, even for the simple case we analyzed, although expected, is not trivial as it demonstrates that the various differential-algebraic constraints are implemented with sufficient accuracy so that spectral accuracy is maintained. Detailed comparisons with DNS and FCM show that the DLM method agrees with both DNS and FCM very well in the region far away from the particle. In regions near and inside the particle it is in good agreement with DNS. These results indicate that the spectral DLM method captures the flow field accurately in both the near and far fields unlike FCM. We note here that FCM can be thought of as a "lumped" version of DLM for which the no-slip condition is not imposed explicitly.

We have only tested relatively simple geometries with a single particle in this first work. Clearly, this is not a limitation of the method and we are currently pursuing more complex problems as well. However, we wanted to focus on well-defined benchmarks that were currently lacking in the DLM literature. We have found, for example, that while the choice of the collocation points on the boundaries is a factor on the accuracy of DLM method, it can be overcome by maintaining nominally regular grids and pursuing p-refinement. We have also demonstrated that we can achieve very high levels of accuracy using DLM with relatively few points.

So far we have concentrated on the *verification* of the new spectral DLM method. We have also considered the *validation* of the method with experimental measurements. Fig. 15 shows the velocity history of a single sphere settling in a channel computed with spectral DLM method and a comparison with the experimental measurement in [25] at Reynolds number $Re_p = 41$ (based on the terminal velocity and the

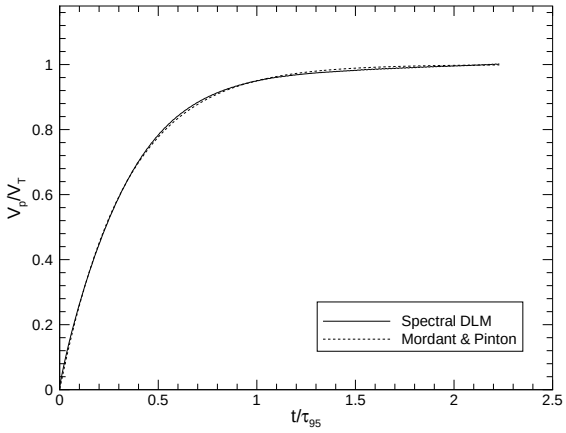

Fig. 15. Sedimentation of a single sphere: sphere velocity versus time from spectral DLM calculation and from experimental measurement by Mordant and Pinton [25] at Reynolds number $Re_p = 41$ based on the terminal velocity and sphere diameter. V_p is sphere velocity; V_T is the terminal velocity; τ_{95} is the time it takes for the sphere to reach 95% of the terminal velocity.

Table 3
Comparison of timing among DNS, FCM and spectral DLM for the flow past a sphere near one wall in a 3D channel (Section 4.7)

	Elements/grid	Processors	Seconds/step	Time steps	Computers
DNS	4608 (5th order)	32	25	6000	IBM SP3
FCM	360 (6th order)	1	16	6000	Pentium 4 PC
DLM	$96 \times 72 \times 96$	16	32	4000	Pentium 3 cluster

"Seconds/step" refers to the wall clock time per time step. "Time steps" records the total number of time steps to convergence.

sphere diameter). The result obtained by spectral DLM is in good agreement with the experimental data, indicating that the new method has captured the unsteady flow accurately in time.

Finally, we comment on the computational complexity of DLM in comparison with other methods. Table 3 lists the wall-clock timing results of the three methods presented in the paper for the sphere flow problem in Section 4.7. In the spectral/*hp* DNS a great deal of resolution and CPU cycles are spent on resolving the flow surrounding the particle. Surprisingly, the cost of spectral DLM method is comparable to that of DNS for particles fixed in space. In [33] an adaptation of the DLM version in [32] is reported, which appears promising in reducing the computational cost of DLM calculations. On the other hand, because FCM does not impose the no-slip condition exactly, it exhibits a significant saving in resolution and computational cost. The true benefit of spectral DLM and potentially superior efficiency over DNS should be expected for many moving particles, for which the cost of DNS based on the ALE formulation will increase substantially whereas the cost of spectral DLM is expected to increase only slightly. Future work will document these cases as well.

Acknowledgements

This work was supported by DARPA, AFOSR and ONR. Computer time was provided by DOD supercomputer centers. We would also like to thank the anonymous referees for helpful suggestions.

References

[1] M. Behr, T.E. Tezduyar, Finite element solution strategies for large-scale flow simulations, Comput. Meth. Appl. Mech. Eng. 112 (1994) 3.
[2] F. Bertrand, P.A. Tanguy, F. Thibault, A three-dimensional fictitious domain method for incompressible fluid problems, Int. J. Numer. Meth. Fluids 25 (1997) 719–736.
[3] M. Briscolini, P. Santangelo, Development of the mask method for incompressible unsteady flows, J. Comput. Phys. 84 (1989) 57.
[4] E.A. Fadlum, R. Vezicco, P. Orlandi, J. Mohd-Yusof, Combined immersed-boundary finite-difference methods for three-dimensional complex flow simulations, J. Comput. Phys. 161 (2000) 35–60.
[5] J. Glimm, J.W. Grove, X.L. Li, W. Oh, D.H. Sharp, A critical analysis of Rayleigh–Taylor growth rates, J. Comput. Phys. 169 (2001) 363.
[6] R. Glowinski, T.W. Pan, T.I. Helsa, D.D. Joseph, A distributed Lagrange multiplier/fictitious domain method for particulate flows, Int. J. Multiphase Flow 25 (1999) 755–794.
[7] R. Glowinski, T.-W. Pan, T.I. Helsa, D.D. Joseph, J. Periaux, A distributed Lagrange multiplier/fictitious domain method for the simulation of flow around moving rigid bodies: application to particulate flow, Comput. Meth. Appl. Mech. Eng. 184 (2000) 241–267.
[8] R. Glowinski, T.W. Pan, T.I. Helsa, D.D. Joseph, J. Periaux, A fictitious domain approach to the direct numerical simulation of incompressible viscous flow past moving rigid bodies: application to particulate flow, J. Comput. Phys. 169 (2001) 363–426.

[9] J.L. Guermond, J. Shen, Velocity-correction projection methods for incompressible flows, SIAM J. Numer. Anal. 41 (2003) 112–134.
[10] P. Hansbo, The characteristic streamline diffusion method for the time-dependent incompressible Navier–Stokes equations, Comput. Meth. Appl. Meth. Eng. 99 (1992) 171.
[11] J.S. Hesthaven, Spectral penalty method, Appl. Numer. Math. 33 (2000) 23–41.
[12] H.H. Hu, Direct simulation of flows of solid-liquid mixtures, Int. J. Multiphase Flow 22 (1996) 335–352.
[13] H.H. Hu, N.A. Patankar, M.Y. Zhu, Direct numerical simulations of fluid–solid systems using the arbitrary Lagrangian–Eulerian technique, J. Comput. Phys. 169 (2001) 427–462.
[14] D. Jacqmin, Calculation of two-phase Navier–Stokes flows using phase-field modeling, J. Comput. Phys. 155 (1999) 96.
[15] D. Jamet, O. Lebaigue, N. Coutris, J.M. Delhaye, The second gradient method for the direct numerical simulations of liquid–vapor flows with phase-change, J. Comput. Phys. 169 (2001) 624.
[16] A. Johnson, T.E. Tezduyar, 3D simulation of fluid–particle interactions with the number of particles reaching 100, Comput. Meth. Appl. Mech. Eng. 145 (1997) 301.
[17] A. Johnson, T.E. Tezduyar, Advanced mesh generation and update methods for 3D flow simulations, Comput. Mech. 23 (1999) 130.
[18] L.H. Juarez, R. Glowinski, T.W. Pan, Numerical simulation of sedimentation of rigid bodies in an incompressible viscous fluid by Lagrange multiplier/fictitious domain methods combined with the Taylor–Hood finite element approximation, J. Sci. Comput. 17 (2002) 683.
[19] G.E. Karniadakis, M. Israeli, S.A. Orszag, High-order splitting methods for the incompressible Navier–Stokes equations, J. Comput. Phys. 97 (1991) 414.
[20] G.E. Karniadakis, S.J. Sherwin, Spectral/hp Element Methods for CFD, Oxford University Press, Oxford, 1999.
[21] R.M. Kirby, T.C. Warburton, S.J. Sherwin, A. Beskok, G.E. Karniadakis, The Nektar code: dynamic simulations without remeshing, In: Proceedings of the Second International Conference on Computational Technologies for Fluid/Thermal/Chemical Systems with Industrial Applications, August 1999.
[22] M.-C. Lai, C.S. Peskin, An immersed boundary method with formal second-order accuracy and reduced numerical viscosity, J. Comput. Phys. 160 (2000) 705–719.
[23] S. Lomholt, B. Stenum, M.R. Maxey, Experimental verification of the force coupling method for particulate flows, Int. J. Multiphase Flow 28 (2002) 225.
[24] P.D. Minev, A stabilized incremental projection scheme for the incompressible Navier–Stokes equations, Int. J. Numer. Meth. Fluids 36 (2001) 441.
[25] N. Mordant, J.-F. Pinton, Velocity measurement of a settling sphere, Eur. Phys. J., B 18 (2000) 343–352.
[26] M.R. Maxey, B.K. Patel, E.J. Chang, L.P. Wang, Simulations of dispersed turbulent multiphase flow, Fluid Dyn. Res. 20 (1997) 143–156.
[27] M.R. Maxey, B.K. Patel, Localized force representations for particle sedimenting in Stokes flow, Int. J. Multiphase Flow 9 (2001) 1603–1626.
[28] S. Osher, R.P. Fedkiw, Level set methods: an overview and some recent results, J. Comput. Phys. 169 (2001) 463.
[29] T.-W. Pan, R. Glowinski, Direct simulation of the motion of neutrally buoyant circular cylinders in plane Poiseuille flow, J. Comput. Phys. 181 (2002) 260–279.
[30] T.-W. Pan, D.D. Joseph, R. Glowinski, Modelling Rayleigh–Taylor instability of a sedimenting suspension of several thousand circular particles in a direct numerical simulation, J. Fluid Mech. 434 (2001) 23–37.
[31] T.-W. Pan, D.D. Joseph, R. Bai, R. Glowinski, V. Sarin, Fluidization of 1204 spheres: simulation and experiment, J. Fluid Mech. 451 (2002) 169–191.
[32] N.A. Patankar, P. Singh, D.D. Joseph, R. Glowinski, T.W. Pan, A new formulation of the distributed Lagrange multiplier/fictitious domain method for particulate flows, Int. J. Multiphase Flow 26 (2000) 1509–1524.
[33] N.A. Patankar, A formulation for fast computations of rigid particulate flows, Center for Turbulence Research, Annual Research Briefs (2001) 185–196.
[34] N.A. Patankar, P.Y. Huang, T. Ko, D.D. Joseph, Lift-off of a single particle in Newtonian and viscoelastic fluids by direct numerical simulation, J. Fluid Mech. 438 (2001) 67.
[35] C.S. Peskin, Flow patterns around heart valves: a numerical method, J. Comput. Phys. 10 (1972) 252.
[36] C.S. Peskin, Numerical analysis of blood flow in the heart, J. Comput. Phys. 25 (1977) 220.
[37] C.S. Peskin, The immersed boundary method, Acta Numerica (2002) 1–39.
[38] A. Prosperetti, H.N. Oguz, Physalis: a new $o(N)$ method for the numerical simulation of disperse systems: potential flow of spheres, J. Comput. Phys. 167 (2001) 196–216.
[39] R. Scardovelli, S. Zaleski, Direct numerical simulation of free-surface and interfacial flow, Ann. Rev. Fluid Mech. 31 (1999) 567.
[40] P. Singh, D.D. Joseph, T.I. Helsa, R. Glowinski, T.-W. Pan, A distributed Lagrange multiplier/fictitious domain method for viscoelastic particulate flows, J. Non-Newtonian Fluid Mech. 91 (2000) 165–188.

[41] M. Sussman, P. Smereka, S. Osher, A level set approach for computing solutions to incompressible two-phase flows, J. Comput. Phys. 114 (1994) 146.
[42] G. Tryggvason, B. Bunner, A. Esmaeeli, D. Juric, N. Al-Rawahi, W. Tauber, J. Han, S. Nas, Y.-J. Jan, A front-tracking method for the computations of multiphase flow, J. Comput. Phys. 169 (2001) 708–759.
[43] T. Yabe, F. Xiao, T. Utsumi, The constrained interpolation profile (CIP) method for multiphase analysis, J. Comput. Phys. 169 (2001) 556.